Title: Assessing the influence of COVID-19 on Earth's radiative balance

Authors: Yi Ming[1]*, Norman G. Loeb[2], Pu Lin[1], Zhaoyi Shen[3], Vaishali Naik[1], Clare E. Singer[3], Ryan X. Ward[3], Fabien Paulot[1], Zhibo Zhang[4,5], Nicolas Bellouin[6], Larry W. Horowitz[1], Paul A. Ginoux[1], V. Ramaswamy[1].

Affiliations:

[1]NOAA/Geophysical Fluid Dynamics Laboratory

[2]NASA/Langley Research Center

[3]Department of Environmental Science and Engineering, California Institute of Technology

[4]Department of Physics, University of Maryland Baltimore County

[5]Joint Center for Earth System Technology, University of Maryland Baltimore County

[6]Department of Meteorology, University of Reading

*Correspondence to: Yi.Ming@noaa.gov.

Abstract: The COVID-19 pandemic led to a widespread reduction in aerosol emissions. Anecdotal effects on air quality and visibility were widely reported. Less known are the impacts on the planetary energy balance. Using satellite observations and climate model simulations, we study the underlying mechanisms of the large, precipitous decreases in solar clear-sky reflection (3.8 W m^{-2} or 7%) and aerosol optical depth (0.16 or 32%) over the East Asian Marginal Seas in March 2020. By separating the impacts due to meteorology and emissions in the model simulations, we find that about one-third of the anomalies can be attributed to pandemic-related emission reductions, and the rest to weather variability and long-term emission trends. The current observational and modeling capabilities will be critical for monitoring, understanding, and predicting the radiative forcing and climate impacts of the ongoing crisis.

One Sentence Summary: The COVID-19-related aerosol emissions reduction caused a significant perturbation to the energy balance over East Asia in March 2020.

Main Text: The lockdown measures instituted to control the spread of COVID-19 caused unprecedented disruptions to many economic sectors, among which manufacturing and transportation were particularly hard hit. The consequent decrease in emissions of anthropogenic aerosols and their precursors generally led to improvements in air quality and visibility (*1*-*3*), with notable exceptions (*4*). These emissions reductions may have had an influence on Earth's radiation budget, and by extension weather and climate, as short-lived aerosol particles have long been postulated to provide a net cooling by scattering/absorbing insolation (direct effects) under clear-sky conditions (*5*-*7*) and brightening clouds (indirect effects) under cloudy conditions (*8, 9*).

Satellite observations (detailed in Materials and Methods) offer some indications. For March 2020, one month after China implemented a strict lockdown, the Moderate Resolution Imaging Spectroradiometer (MODIS) aerosol optical depth (AOD) (*10*) exhibited large negative anomalies relative to the climatological (2003–2019) mean, not only over much of East Asia, but also extending downwind over the Pacific (Fig. 1A). The average decrease over the East Asian Marginal Seas (EAMS) (defined as the oceanic region in 117°–132°E and 26°–41°N) was 0.16,

or 32% of the climatological mean (Fig. 1B). We choose EAMS as the main analysis region for its proximity to the upwind source regions, more reliable satellite retrievals over ocean than over land (*11*), and absence of surface snow/ice cover. The concurrently measured Clouds and the Earth's Radiant Energy System (CERES) Energy Balanced and Filled (EBAF) shortwave clear-sky top-of-the-atmosphere (TOA) radiative flux (F_{clr}, upward defined as positive) (*12*) was also greatly reduced during March 2020 (Fig. 1C). The average decrease over EAMS was 3.8 W m^{-2}, or 7% (Fig. 1D). Both anomalies exceed their respective 90% confidence intervals (Figs. 1B and 1D), and the two quantities are strongly correlated on interannual timescales (Fig. S1A). This suggests that a substantial emissions reduction, presumably caused by COVID-19, gave rise to lower aerosol loading, resulting in more solar absorption by Earth's surface.

There are, however, inherent difficulties in interpreting the observations. Besides emissions, meteorology plays a prominent role in modulating AOD and F_{clr}, especially outside of source regions, via multiple pathways (e.g. long-range transport, hygroscopic growth, and wet removal). For instance, the negative anomalies over EAMS in March 2005, when there was no anomalous emissions reduction, were comparable to those in March 2020 (Figs. 1B and 1D). Therefore, a confident attribution of the observed decreases in AOD and F_{clr} to the emissions reduction hinges on a reliable approach for isolating the non-COVID-19 factors. It is even more challenging to discern possible impacts on shortwave all-sky TOA radiative flux (F_{all}) due to the complexities involving clouds.

We address these issues by using the latest GFDL atmosphere global climate model (GCM) AM4 (*13*), which participated in the World Climate Research Programme (WCRP) Coupled Model Intercomparison Project Phase 6 (CMIP6) (*14*) and forms the basis of a climate prediction system (*15*). Instead of generating its own meteorology (typical of climate simulations), the model is nudged to re-analysis data (winds, air temperature and surface pressure) at all levels to create a meaningful comparison with observations at synoptic scales. Still, aerosols, water vapor, and clouds are computed interactively and subject to the same dynamical and physical processes as in a free-running simulation, posing a stringent test for model physics. The time evolution of anthropogenic emissions over China is depicted in Fig. S2. After peaking in 2007, SO_2 has been decreasing steadily due to air pollution control measures, while black carbon (BC) and organic matter (OM) diverged after 2015, compensating each other to some extent. (The model setup and experimental design are detailed in Materials and Methods.)

The nudged control simulation shows considerable skill in reproducing the observed interannual variations of AOD and F_{clr} for March over EAMS; the correlation coefficients (r) between model and observations are 0.83 and 0.72, respectively (Fig. 2). [The model performance is comparable for the other months (Fig. S3).] This suggests that the nudged AM4 provides an effective way to quantify the non-COVID-19 influence. The most notable deficiency is that the simulation does not capture the full extents of the negative anomalies in March 2005. However, the model-simulated AOD and F_{clr} anomalies are strongly correlated (Fig. S1B), with a slope that is very close to the observationally-based counterpart (Fig. S1A). This lends support to the fidelity of the model's representation of the aerosol direct effects. Both observed anomalies emerge from the lower bounds of the detection limits, meaning that they are likely to contain forced components [estimated at -0.06 for AOD (1.9 standard deviations) and -1.3 W m^{-2} for F_{clr} (1.3 standard deviations) by subtracting the control values from the respective observations]. The likelihood is 92% for AOD, and 80% for F_{clr}. When compared with the

perturbation simulations, the observations are consistent with a 40-60% anthropogenic emissions reduction over China (relative to 2020), which roughly translates into a reduction of 31-47% in SO_2 emissions relative to 2015, as the baseline SO_2 emissions in 2015 are 28% higher than in 2020 (Fig. S2A). Note that SO_2 is the major contributor to the forced change in F_{clr} (see Supplementary Text). Further, it is important to note that this top-down estimate is obtained in a way that is fundamentally different from, but complementary to, conventional bottom-up approaches based on socioeconomic data. One study of the latter kind (*16*) suggests that SO_2 emissions over China decreased by about 20% in March 2020 (relative to 2015). Given the complicated nature of producing such bottom-up estimates, it is not expected that they should agree perfectly with our result. Moreover, the responses of AOD and F_{clr} over EAMS are somewhat sensitive to the location of the emissions reduction (see Supplementary Text). It may help reconcile the difference between the two types of estimates to take into account the precise spatiotemporal pattern of the emissions reduction, once known.

We choose the 60% perturbation simulation to illustrate the spatial distributions of the model-simulated AOD and F_{clr} anomalies in Fig. 3. (Fig. S4 is the same plot for the 40% perturbation simulation.) The simulation exhibits a clear land-sea contrast; the large AOD anomaly over mainland China decreases gradually down the prevailing southwesterlies over the ocean (Fig. 3A). This pattern is in broad agreement with MODIS (Fig. 1A). The overall anomaly can be decomposed into the part due to both the meteorology and long-term emission trends (non-COVID-19) and into the part due to the COVID-19-related emissions reduction. The former is the anomaly in the control simulation (Fig. 3B), and the latter is the difference between the 60% perturbation and control simulations (Fig. 3C). The two contributors to the overall anomaly are of comparable magnitudes, but show different spatial patterns. For instance, the plume cutting across northern China, the Korean Peninsula and northern Japan in the non-COVID-19 component is not present in the COVID-19 counterpart. The impact of COVID-19 on AOD is concentrated over southern China. These features largely carry over to F_{clr} (Figs. 3D-F). The aforementioned decomposition yields insights into the physical mechanisms of regional anomalies. An example is the dipole structure immediately north of the northern boundary of EAMS (41°N), characteristic of the large positive anomalies over parts of Inner Mongolia and Mongolia and the negative anomalies over Northeast China. It can be attributed to meteorology as it exists only in the non-COVID-19 component, realized through land surface albedo changes caused by snow melting or accumulation (not shown). A notable discrepancy is that the model projects a large decrease in F_{clr} over much of China (Fig. 3D), which is not found in the CERES observations (Fig. 1C). Although the underlying cause is not entirely clear, it is difficult to reconcile the substantial decrease in MODIS AOD over northern China with the lack of any significant change in CERES F_{clr} over the same region given the strong correlation between them (Fig. S1A).

Excellent agreement (r=0.94) is seen between CERES and AM4-simulated shortwave all-sky flux (F_{all}) (Fig. 4A). This result is somewhat counterintuitive since F_{all} is under the heavy influence of clouds, which GCMs historically have struggled to simulate owing to the intrinsic difficulties in representing the effects of cloud-scale turbulence in coarse-resolution models. We cross-check this result by comparing the modeled cloud fraction with CERES observations (Fig. 4B). The equally impressive model skill (r=0.92) affirms the prominent role of atmospheric motion in dictating cloud fraction and the quality of AM4's cloud scheme (*17, 18*). (More work is needed to better understand the contributions from different cloud types.) The

negative anomaly in F_{all} (-2.1 W m^{-2}) for March 2020 is just within the detection limit, while the negative anomaly in cloud fraction is barely outside. Interestingly, MODIS cloud fraction shows a much larger negative anomaly than its CERES counterpart (Fig. 4B). Although the sign of the model-simulated forced signal in F_{all} (less reflection) in the 60% perturbation simulation is consistent with our expectation for a COVID-19-related emissions reduction, the magnitude (-0.5 W m^{-2}) is well within the detection limit. One may interpret this discrepancy as an indication that the model underestimates the strength of the aerosol indirect effects since the clear-sky results substantiate the scale of the emissions reduction and the realism of the direct effects. There is, however, no clear signal in MODIS-retrieved cloud effective radius (R_e) (Fig. 4C) or liquid water path (LWP) (Fig. 4D). A previous study of the cloud response to volcanic aerosols (*19*) found a strong anomaly in MODIS R_e, but not in LWP. The main model used in that study (HadGEM3), when nudged, did not reproduce the observed interannual variations in R_e (see Figs. S4.1-S4.4 in that study), so there was no reliable way to separate forced signal from weather variability, making it hard to interpret the observed anomaly. The AM4-simulated R_e does not correlate with MODIS either, but this is not central to our argument. The model has limited skill for LWP (Fig. 4D), but the anomaly in MODIS LWP for March 2020 falls within the detection limit, at least partly owing to the uncertainty in MODIS LWP (*20*). For instance, MODIS ascribes the large positive anomaly in cloud fraction for March 2010 primarily to ice clouds, as opposed to liquid clouds. As a consequence, there is little change in MODIS LWP. By contrast, the model-simulated cloud fraction and LWP are strongly correlated. Although this is not ground for a critique of MODIS LWP retrieval, the model result in and of itself should be taken seriously in light of AM4's demonstrated skill and self-consistency. In summary, our all-sky analyses indicate that the observed negative anomaly in F_{all} for March 2020 was likely caused by weather variability. While nominally consistent with the all-sky radiative impacts of an emissions reduction, it was realized through lower cloud fraction, instead of higher R_e or lower LWP, the two main pathways through which the aerosol indirect effects manifest in GCMs (including AM4).

A series of additional simulations and analyses are conducted to assess the robustness of the key findings for March 2020. They cover the analysis region, long-term emission trends, and locations and speciation of the emissions reduction. Although quantitative differences exist, the main conclusions remain valid regardless of specific choices or settings (see Figs. S5-S15 and Supplementary Text).

We carry out the same analyses for February and April (Figs. S16-S19). The MODIS AOD in February 2020 is the lowest since 2005 (Fig. S16). The control simulation projects a negative anomaly in 2020, but of only half of the observed magnitude. The discrepancy can be accounted for by a 20-40% emissions reduction. In terms of F_{clr}, the model is less skillful for February than for March, resulting in a larger detection limit. Unlike AOD, the observed F_{clr} falls within the limit. Note that the observed F_{clr} is not nearly as variable as the observed AOD in the few years before 2020, breaking the tight linkage between the two quantities for March (Fig. S1A). Since the physics governing the AOD-F_{clr} relationship is simple and robust, more needs to be done to reconcile the two retrievals. One possibility is compensation between scattering and absorbing aerosols. Both the observed F_{all} and cloud fraction anomalies are smaller than those in the control simulation (qualitatively similar to March), but within their respective detection limits (Fig. S17).

Any sign of AOD decrease is gone by April. Although the MODIS AOD is anomalously low in April 2020, the fact that it is very close to the control suggests no significant COVID-19-related emissions reduction (Fig. S18). This inference is supported by the observed F_{clr}, which is slightly above the upper bound of the detection limit, opposite to the perturbation simulations. *In stark contrast, the observed F_{all} shows an outsized negative anomaly of XXX W m^{-2}, the largest in the entire CERES data record (Fig. S19). This coincides with the largest decrease in CERES cloud fraction. The control simulation captures the timing and magnitude of both anomalies, allowing us to attribute them to the specific meteorological conditions in April 2020, as opposed to the anthropogenic aerosol effects.* **[NOTE TO EDITOR and REVIEWERS: The preceding three sentences in italic are placeholders as the CERES all-sky data for April 2020 have not been released. They will be re-visited after the data are available in early August.]** The above findings are consistent with a recent study of CO_2 emissions during COVID-19 (*21*), which suggests that the emissions over China decreased substantially in February and March 2020, but almost fully recovered by April.

The COVID-19 pandemic provides an opportunity for evaluating the model representation of the aerosol-cloud-radiation interactions, a major source of uncertainty in global weather and climate modeling. The observational evidence for aerosol direct effects is unequivocal, and their model representation is satisfactory. In contrast, it is more difficult to draw definitive conclusions about aerosol-cloud interactions and indirect effects from the observed shortwave all-sky flux. This is fundamentally due to the highly variable, fine-scale nature of clouds, the challenges in retrieving cloud properties on the observational side, and in parameterizing sub-grid cloud processes on the modeling side. Nonetheless, the fact that both the model-simulated perturbations and the observations stay within the detection limits leads us to conclude that there is no evidence suggesting that the model-simulated aerosol indirect effects are too strong. The observations underline the dominant role of cloud fraction in determining the all-sky flux. Any attempt at discerning the manifestation of the aerosol indirect effects through cloud microphysical properties (such as R_e and LWP) is contingent on separating out interference from the synoptic-scale variations in cloud fraction.

Running in the nudged mode to separate the effects of meteorology from emissions, AM4 is skillful at reproducing the observed interannual variations in shortwave TOA radiative fluxes, clear and cloudy-sky alike. This allows us to distinguish forced signal from weather variability, a prerequisite for interpreting observations. We find that about one-third of the observed decrease in shortwave clear-sky reflection over East Asian Marginal Seas (1.3 out of 3.8 W m^{-2} locally) in March 2020 was likely caused by COVID-19-related emissions reduction. On the other hand, the concurrent decrease in shortwave all-sky reflection (2.1 W m^{-2}) is within the detection limit, and thus is thought to be caused mainly by weather variability. By leveraging the latest observational and modeling capabilities, the framework described here is ideal for studying the radiative impacts of the ongoing COVID-19 pandemic, and the resulting perturbations to the energy balance, in other parts of the world (such as Europe and North America).

References and Notes:

1. S. Mahato, S. Pal, K. G. Ghosh, Effect of lockdown amid COVID-19 pandemic on air quality of the megacity Delhi, India. *Sci Total Environ*. **730**, (2020), 10.1016/j.scitotenv.2020.139086.

2. S. Sharma, M. Zhang, Anshika, J. Gao, H. Zhang, S. Kota, Effect of restricted emissions during COVID-19 on air quality in India. *Sci Total Environ*. **728**, (2020), 10.1016/j.scitotenv.2020.138878.
3. V. F. McNeill, COVID-19 and the Air We Breathe. *ACS Earth and Space Chem.* **4**(5), 674, (2020), 10.1021/acsearthspacechem.0c00093.
4. T. Le, Y. Wang, L. Liu, J. Yang, Y. Yung, G. Li, Guohui, J. Seinfeld, Unexpected air pollution with marked emissions reductions during the COVID-19 outbreak in China. *Science*, (2020), 10.1126/science.abb7431.
5. J. M. J. Mitchell, The effect of atmospheric aerosols on climate with special reference to temperature near the earth's surface. *J Appl Meteorol*. **10**, 703, (1971).
6. J. M. Haywood, V. Ramaswamy, B. J. Soden, Tropospheric aerosol climate forcing in clear-sky satellite observations over the oceans. *Science*, **283**(5406), 1299, (2009), 10.1126/science.283.5406.1299.
7. N. Bellouin, O. Boucher, D. Tanré, O. Dubovik, Aerosol absorption over the clear-sky oceans deduced from POLDER-1 and AERONET observations. *Geophy Res Lett*, **30**(14), 1748, (2003), 10.1029/2003GL017121.
8. S. Twomey, Pollution and the planetary albedo. *Atmos Environ*, **8**(12), 1251 (1974).
9. B. A. Albrecht, Aerosols, cloud microphysics, and fractional cloudiness. *Science*, **245**(4923), 1227, (1989).
10. L. A. Remer, Y. J. Kaufman, D. Tanré, S. Mattoo, D. A. Chu, J. V. Martins, R.-R. Li, C. Ichoku, R. C. Levy, R. G. Kleidman, T. F. Eck, E. Vermote, B. N. Holben, The MODIS Aerosol Algorithm, Products and Validation. *J Atmos Sci*. **62**(4), 947, (2005), doi:10.1175/JAS3385.1.
11. N. C. Hsu, M.-J. Jeong, C. Bettenhausen, A Sayer, R. Hansell, C. Seftor, J. Huang, S. C. Tsay, Enhanced Deep Blue aerosol retrieval algorithm: The second generation. *J Geophys Res Atmos*. **118**, (2013), 10.1002/jgrd.50712.
12. N. Loeb, D. Doelling, H. Wang, W. Su, C. Nguyen, J. Corbett, L. Liang, C. Mitrescu, F. Rose, S. Kato, Clouds and the Earth's Radiant Energy System (CERES) Energy Balanced and Filled (EBAF) top-of-atmosphere (TOA) edition-4.0 data product. *J Clim.* **31**, (2017), 10.1175/JCLI-D-17-0208.1.
13. M. Zhao, J.-C. Golaz, I. M. Held, H. Guo, V. Balaji, R. Benson, J.-H. Chen, X. Chen, L. J. Donner, J. P. Dunne, K. Dunne, J. Durachta, S.-M. Fan, S. M. Freidenreich, S. T. Garner, P. Ginoux, L. M. Harris, L. W. Horowitz, J. P. Krasting, A. R. Langenhorst, Z. Liang, P. Lin, S.-J. Lin, S. L. Malyshev, E. Mason, P. C. D. Milly, Y. Ming, V. Naik, F. Paulot, D. Paynter, P. Phillipps, A. Radhakrishnan, V. Ramaswamy, T. Robinson, D. Schwarzkopf, C. J. Seman, E. Shevliakova, Z. Shen, H. Shin, L. G. Silvers, J. R. Wilson, M. Winton, A. T. Wittenberg, B. Wyman, B. Xiang, The GFDL Global Atmosphere and Land Model AM4.0/LM4.0: 1. Simulation Characteristics With Prescribed SSTs. *J Adv Model Earth Syst.* **10**, 691, (2018).
14. V. Eyring, S. Bony, G. A. Meehl, C. A. Senior, B. Stevens, R. J. Stouffer, K. E. Taylor, Overview of the Coupled Model Intercomparison Project Phase 6 (CMIP6) experimental design and organization, *Geosci Model Dev*, **9**, 1937, (2016).
15. T. Delworth, W. Cooke, A. Adcroft, M. Bushuk, J.-H. Chen, K. Dunne, P. Ginoux, R. Gudgel, R. Hallberg, L. Harris, M. Harrison, N. Johnson, S. Kapnick, S.-J. Lin, F. Lu, S.

Malyshev, P. Milly, H. Murakami, V. Naik, M. Zhao, SPEAR: The Next Generation GFDL Modeling System for Seasonal to Multidecadal Prediction and Projection. *J Adv Model Earth Syst.* **12**, (2020), 10.1029/2019MS001895.

16. P. M. Forster, H. I. Forster, M. J. Evans, M. J. Gidden, C. D. Jones, C. A. Keller, R. Lamboll, C. Le Quéré, J. Rogelj, D. Rosen, C.-F. Schleussner, T. B. Richardson, C. J. Smith, S. T. Turnock, Current and future global climate impacts resulting from COVID-19, submitted.
17. O. Boucher, J. Servonnat, A. L. Albright, O. Aumont, Y. Balkanski, V. Bastrikov, et al., Presentation and evaluation of the IPSL-CM6A-LR climate model. *J. Adv. Model. Earth Syst*. **12**, (2020), 10.1029/2019MS002010.
18. N. G. Loeb, H. Wang, R. P. Allan, T. Andrews, K. Armour, J. N. S. Cole, J.-L. Dufresne, P. M. D. Forster, A. Gettelman, H. Guo, T. Mauritsen, Y. Ming, D. J Paynter, C. Proistosescu, M. F. Stuecker, U. Willén, K. Wyser, New Generation of Climate Models Track Recent Unprecedented Changes in Earth's Radiation Budget Observed by CERES. *Geophy Res Lett*. **47**(5), (2020), 10.1029/2019GL086705.
19. F. Malavelle, J. Haywood, A. Jones, A. Gettelman, L. Clarisse, S. Bauduin, R. Allan, I. Karset, J. Kristjánsson, L. Oreopoulos, N. Cho, D. Lee, N. Bellouin, O. Boucher, D. Grosvenor, K. Carslaw, S. Dhomse, G. Mann, A. Schmidt, T. Thordarson, Strong constraints on aerosol–cloud interactions from volcanic eruptions. *Nature*. **546**, 485, (2017), 10.1038/nature22974.
20. J. Leinonen, M. D. Lebsock, G. L. Stephens, K. Suzuki, 2016: Improved Retrieval of Cloud Liquid Water from CloudSat and MODIS. *J Appl Meteor Climatol*, **55**, 1831, (2016), 10.1175/JAMC-D-16-0077.1.
21. C. Le Quéré, R. B. Jackson, M. W. Jones, Adam J. P. Smith, Sam Abernethy, Robbie M. Andrew, Anthony J. De-Gol, David R. Willis, Yuli Shan, Josep G. Canadell, Pierre Friedlingstein, Felix Creutzig, Glen P. Peters, Temporary reduction in daily global CO_2 emissions during the COVID-19 forced confinement. *Nat Clim Chang*, (2020), 10.1038/s41558-020-0797-x.
22. C. M. Polashenski, J. E. Dibb, M. G. Flanner, J. Y. Chen, Z. R. Courville, A. M. Lai, J. J. Schauer, M. M. Shafer, M. Bergin, Neither Dust nor Black Carbon Causing Apparent Albedo Decline in Greenland's Dry Snow Zone: Implications for MODIS C5 Surface Reflectance. *Geophys Res Lett*, **42** (21), 9319, (2015), 10.1002/2015GL065912.
23. R. Gelaro, coauthors, The Modern-Era Retrospective Analysis for Research and Applications, Version 2 (MERRA-2). *J Climate*, **30**, 5419, (2017), 10.1175/JCLI-D-16-0758.1.
24. K. E. Taylor, D. Williamson, F. Zwiers, The sea surface temperature and sea ice concentration boundary conditions for AMIP II simulations. PCMDI Report 60, Program for Climate Model Diagnosis and Intercomparison, Lawrence Livermore National Laboratory, 25 pp, (2000).
25. R. W. Reynolds, N. A. Rayner, T. M. Smith, D. C. Stokes, W. Wang, An improved in situ and satellite SST analysis for climate. *J Climate*, **15**, 1609, (2002).
26. Q. Zhang, D. G. Streets, G. R. Carmichael, K. B. He, H. Huo, A. Kannari, Z. Klimont, I. S. Park, S. Reddy, J. S. Fu, D. Chen, L. Duan, Y. Lei, L. T. Wang, Z. L. Yao, Z. L., Asian

emissions in 2006 for the NASA INTEX-B mission. *Atmos Chem Phys*, **9**, 5131, (2009), 10.5194/acp-9-5131-2009.

27. R. M. Hoesly, S. J. Smith, L. Feng, Z. Klimont, G. Janssens-Maenhout, T. Pitkanen, J. J. Seibert, coauthors, Historical (1750-2014) anthropogenic emissions of reactive gases and aerosols from the Community Emission Data System (CEDS). *Geosci Model Dev*, **11,** 369, (2018).
28. F. Paulot, D. Paynter, P. Ginoux, V. Naik, L. W. Horowitz, Changes in the aerosol direct radiative forcing from 2001 to 2015: observational constraints and regional mechanisms, *Atmos Chem Phys*, **18**, 13265, (2018), 10.5194/acp-18-13265-2018.
29. B. C. O'Neill, C. Tebaldi, D. P. van Vuuren, V. Eyring, P. Friedlingstein, G. Hurtt, R. Knutti, E. Kriegler, J.-F. Lamarque, J. Lowe, G. A. Meehl, R. Moss, K. Riahi, B. M. Sanderson, The Scenario Model Intercomparison Project (ScenarioMIP) for CMIP6. *Geosci Model Dev*, **9**, 3461, (2016), 10.5194/gmd-9-3461-2016.

Acknowledgments: We thank L. Donner and D. Paynter for their helpful comments on an early draft. **Funding:** Z.S. acknowledges support from the Ronald and Maxine Linde Challenge for Climate Science Fund. C.E.S. acknowledges support from the NSF Graduate Research Fellowship under Grant No. DGE-1745301. R.X.W. acknowledges fellowship support from the Resnick Sustainability Institute at Caltech. **Author contributions:** Y.M. and N.G.L. designed the study. P.L and Z.S carried out the simulations and analyzed the model results. V.N. and F.P. provided emission estimates. Z.S, C.E.S., R.X.W., and Z.Z. analyzed the satellite data. Y.M. wrote the manuscript. All authors contributed to the scientific discussions and preparation of the manuscript. **Competing interests:** The authors declare no competing interests. **Data and materials availability:** The AQUA/MODIS MYD08 L3 Global 1 Deg. dataset was acquired from the Level-1 and Atmosphere Archive and Distribution System (LAADS) Distributed Active Archive Center (DAAC), located in the Goddard Space Flight Center in Greenbelt, Maryland (https://ladsweb.nascom.nasa.gov/). The CERES data were obtained from the NASA Langley Research Center Atmospheric Science Data Center (https://doi.org/10.5067/TERRA-AQUA/CERES/EBAF-TOA_L3B004.1). AM4 simulation results are available from the authors upon request.

Supplementary Materials:

Materials and Methods

Fig. S1. Scatter plots of the anomalies in AOD and F_{clr} in March over EAMS. Open dots represent the climatological period (2003-2019) and solid dots represent the year 2020. (A) Observations from MODIS and CERES. (B) Blue dots are from the control model simulation. Orange, green, and red dots correspond to the 20%, 40% and 60% perturbation simulations, respectively. The regression line is calculated for the climatological period.

Fig S2. Time series of monthly-mean anthropogenic emissions over China. (A) SO_2, (B) black carbon (BC), and (C) organic matter (OM).

Fig S3. Time series of monthly anomalies in (A) AOD, (B) F_{clr}, and (C) F_{all}. The black and blue lines represent the observations and the control simulation, respectively. The dotted and solid lines represent the monthly anomalies and 11-month running means, respectively. r is the correlation coefficient.

Fig S4. Same as Fig. 3, but for the 40% perturbation simulation.

Fig S5. Same as Fig. 2, but for the expanded oceanic region from 117°–150°E and 26°–41°N.

Fig S6. Same as Fig. 4, but for the expanded oceanic region from 117°–150°E and 26°–41°N.

Fig S7. Same as Fig. 2, but for the constant emission simulation (the purple line). The blue line is from the control simulation. r is the correlation coefficient for the constant emission simulation.

Fig S8. Same as Fig. 4, but for the constant emission simulation (the purple line). The blue line is from the control simulation. r is the correlation coefficient for the constant emission simulation.

Fig S9. Same as Fig. 2, but for the emission location simulations. NC, CC, and SC represent northern China (north of 35°N), central China (25°–35°N) and southern China (south of 25°N), respectively. The regional emissions reduction is 60%.

Fig S10. Same as Fig. 3, but for the northern China (NC) emission location simulation. The regional emissions reduction is 60%.

Fig S11. Same as Fig. 3, but for the central China (CC) emission location simulation. The regional emissions reduction is 60%.

Fig S12. Same as Fig. 3, but for the southern China (SC) emission location simulation. The regional emissions reduction is 60%.

Fig S13. Same as Fig. 4, but for the emission location simulations. NC, CC, and SC represent the northern China (north of 35°N), central China (25°–35°N) and southern China (south of 25°N), respectively. The regional emissions reduction is 60%.

Fig S14. Same as Fig. 2, but for the emission speciation simulations. The emissions reduction is 60%.

Fig S15. Same as Fig. 4, but for the emission speciation simulations. The emissions reduction is 60%.

Fig S16. Same as Fig. 2, but for February.

Fig S17. Same as Fig. 4, but for February.

Fig S18. Same as Fig. 2, but for April.

Fig S19. Same as Fig. 4, but for April.

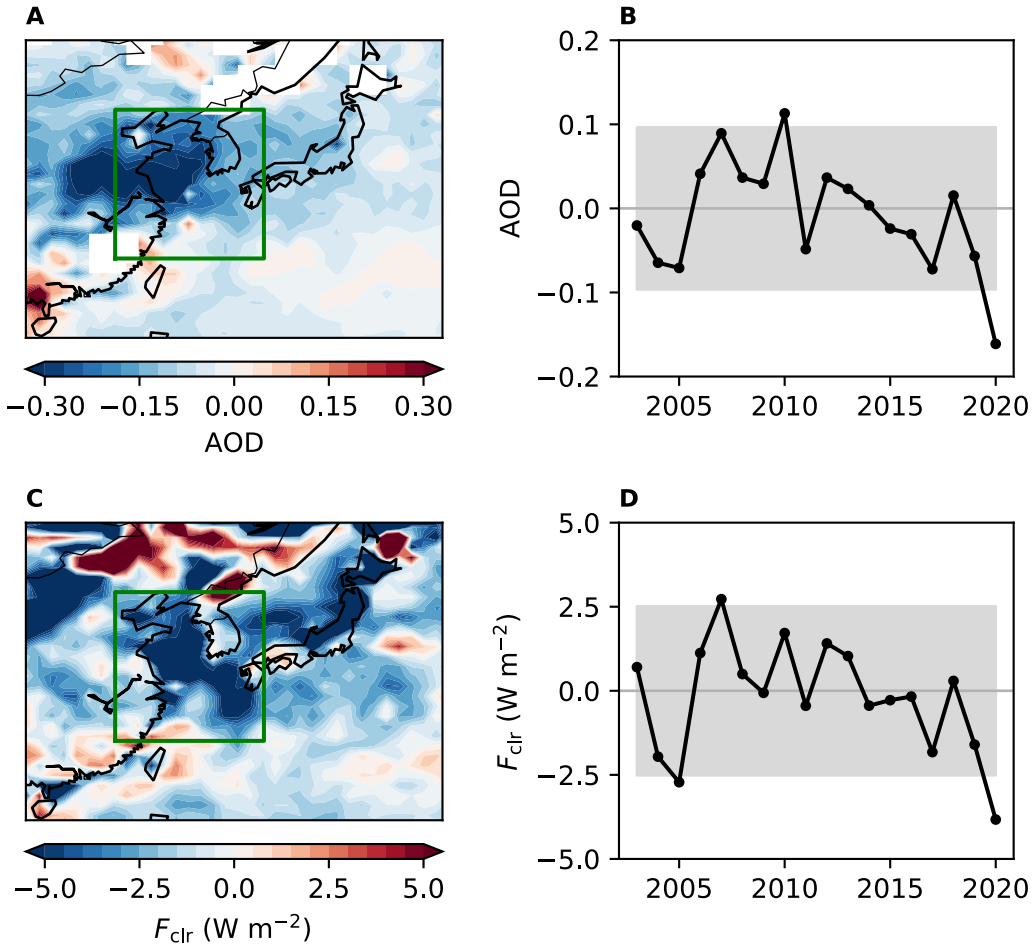

Fig. 1. Satellite measurements of AOD and F_{clr}. (A) Spatial distribution of the anomaly in MODIS aerosol optical depth (AOD) in March 2020. The oceanic region enclosed by the green rectangle (117°–132°E and 26°–41°N) is defined as the East Asian Marginal Seas (EAMS). (B) Time series of the anomaly in MODIS AOD over EAMS in March from 2003 to 2020. The gray area denotes the 90% confidence interval over the climatological period. (C) Same as (A), but for CERES shortwave clear-sky top-of-the-atmosphere (TOA) radiative flux (F_{clr}, upward defined as positive). (D) Same as (B), but for CERES F_{clr}. The climatology is defined as 2003–2019.

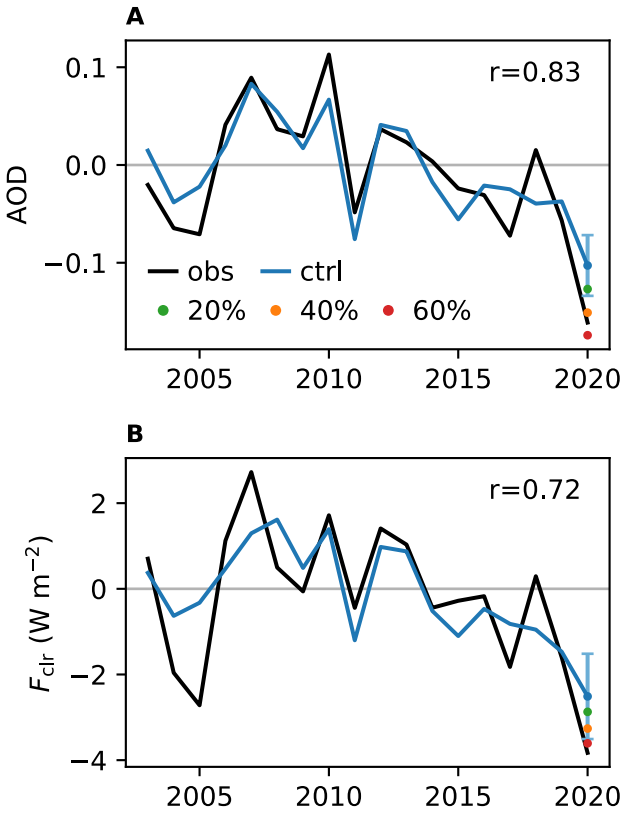

Fig 2. Comparison of the observations and simulations under clear-sky conditions. (A) Times series of the anomaly in AOD over EAMS in March from 2003 to 2020. The black line is from MODIS, and the blue line is from the control simulation. The vertical bar denotes the detection limit (one standard deviation of the differences between the observations and the control simulation from 2003-2019). The orange, green, and red dots denote the perturbation simulations of 20%, 40%, and 60% emissions reductions, respectively. r is the correlation coefficient. (B) Same as (A), but for CERES F_{clr}.

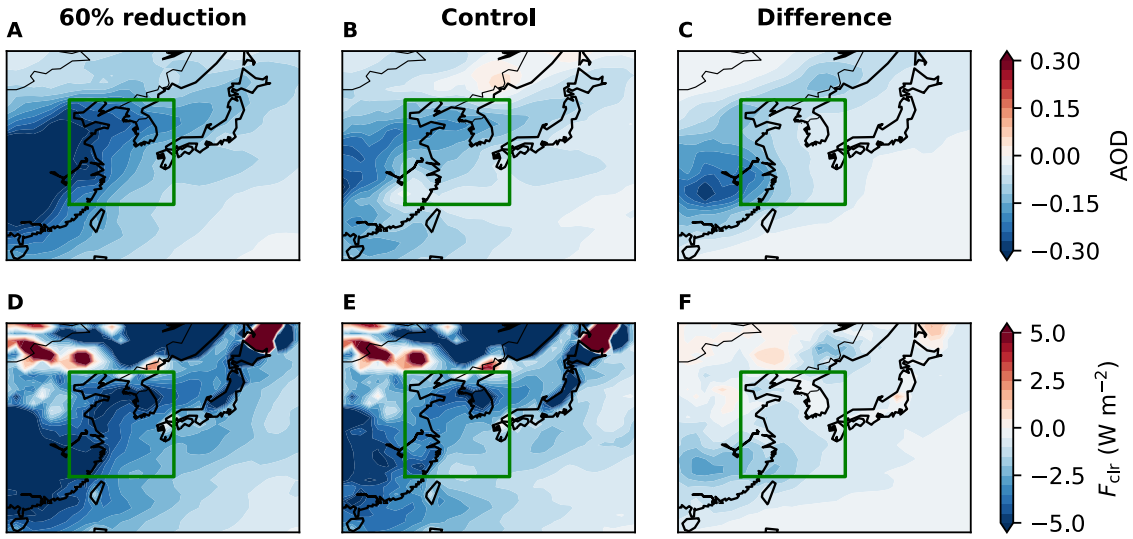

Fig 3. Model simulation of spatial distribution of AOD and F_{clr}. (A) Spatial distribution of the anomaly in AOD in March 2020 from the 60% perturbation simulation. The green rectangle denotes EAMS. (B) Same as (A), but for the control simulation. (C) The difference between (A) and (B). (D)-(F) Same as (A)-(C), but for simulated F_{clr}.

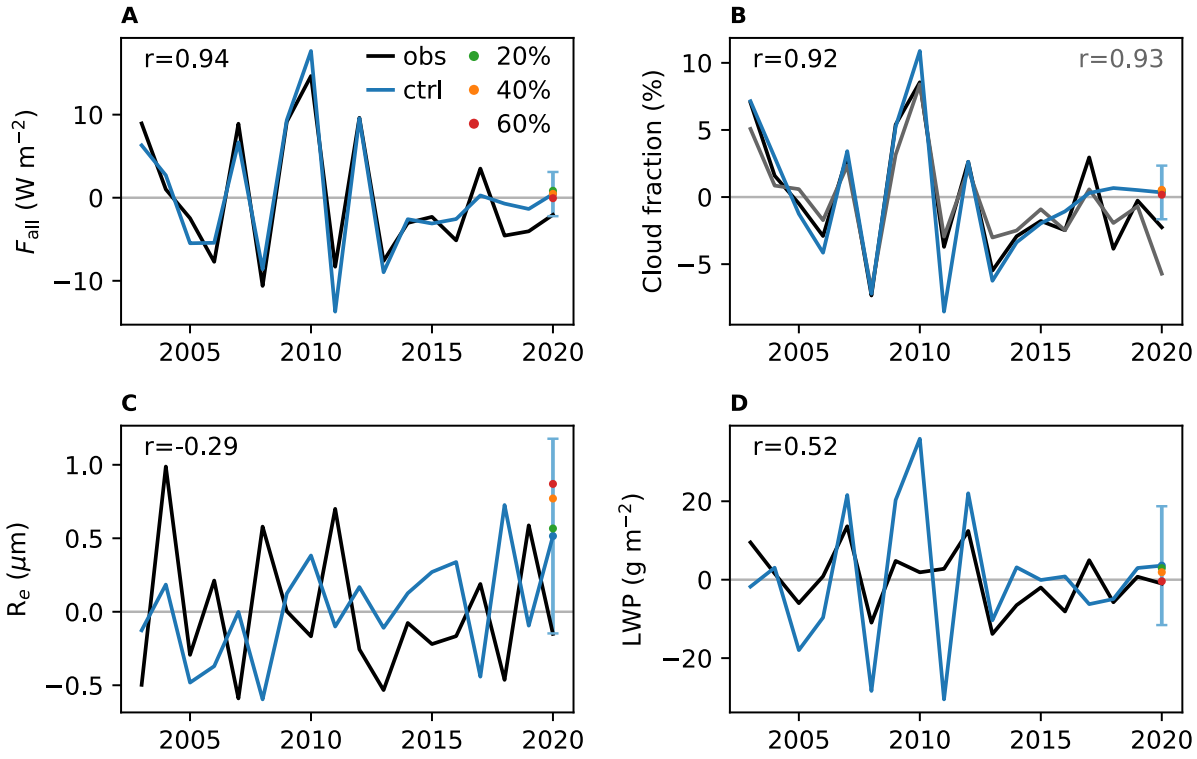

Fig 4. Comparison of the observations and simulations in all-sky conditions. (A) Time series of the anomaly in shortwave all-sky TOA radiative flux (F_{all}) over EAMS in March from 2003 to 2020. The black line is from CERES, and the blue line is from the AM4 control simulation. The vertical bar denotes the detection limit (one standard deviation of the differences between the observations and the control simulation from 2003 to 2019). The orange, green, and red dots denote the perturbation simulations of 20%, 40% and 60% emissions reductions, respectively. r is the correlation coefficient. (B) Same as (A), but for cloud fraction. The black line is from CERES, and the gray line is from MODIS. The detection limit is based on CERES. (C) Same as (A), but for cloud effective radius (R_e). The black line is from MODIS. (D) Same as (A), but for liquid water path (LWP). The black line is from MODIS.

Supplementary Materials for

Assessing the influence of COVID-19 on Earth's radiative balance

Yi Ming[1]*, Norman G. Loeb[2], Pu Lin[1], Zhaoyi Shen[3], Vaishali Naik[1], Clare E. Singer[3], Ryan X. Ward[3], Fabien Paulot[1], Zhibo Zhang[4,5], Nicolas Bellouin[6], Larry W. Horowitz[1], Paul A. Ginoux[1], V. Ramaswamy[1].
Correspondence to: Yi.Ming@noaa.gov

This PDF file includes:

Materials and Methods

Satellite observations

We use the observed shortwave top-of-atmosphere (TOA) fluxes and cloud fraction from the Clouds and the Earth's Radiant Energy System (CERES). Observational data for aerosol and cloud properties are retrieved from the Moderate Resolution Imaging Spectroradiometer (MODIS) instrument aboard NASA's Aqua satellite. While similar products are available from NASA's Terra satellite, others have reported the degradation of the on-board MODIS instrument over time, specifically with respect to the cloud properties of interest in this work (*9*, *22*). All data are Level 3 (L3) monthly products from MODIS Collection 6.1. The L3 monthly product (MYD08_M3) are gridded to 1° by 1° and derived from the daily products (MYD08_D3), made available through NASA's Level-1 and Atmosphere Archive and Distribution System (LAADS) Distribution Active Archive Center (DAAC). The aerosol optical depth (AOD), cloud fraction, cloud effective radius (R_e), and liquid water path (LWP) are retrieved from the MYD08_M3 data set. AOD is derived from the combined Dark Target and Deep Blue AOD at 0.55 μm over the land and ocean. LWP is retrieved from the 3.7 μm band and represents in-cloud properties. To compare with model outputs, the in-cloud LWP is converted to a grid-box mean LWP by multiplying the in-cloud LWP by the liquid cloud fraction (calculated from the mean cloud fraction and cloud phase properties). The observational data are interpolated to the AM4 grid for analysis.

Model simulations

We conduct a suite of nudged simulations from January 2000 to April 2020 with the GFDL AM4 (*11*). The model horizontal winds, temperature, and surface pressure are nudged to the 3-hourly averaged products from the MERRA-2 reanalysis (*23*) with a nudging time scale of 6 hours. The simulations use the monthly sea surface temperatures (SST) and sea ice concentrations prepared for the CMIP6 historical AMIP simulations (*24*), which are extended to 2020 using the NOAA Optimum Interpolation (OI) SST V2 data (*25*).

Aerosol concentrations are calculated interactively based on their emissions, chemistry, advection, and dry and wet deposition. The SO_2 and black carbon (BC) emissions for 2000-2015 used in the control simulations are based on the regional Multi-resolution Emission Inventory for China (MEIC) (*26*) in China and the CMIP6 (Coupled Model Intercomparison Project Phase 6) historical emissions (*27*) in the rest of the world. The latter is not used for China because it severely underestimates the decline of SO_2 after 2007 (*28*). (Note that MEIC ends in 2015.) The SO_2 and BC emissions for 2019 are derived by linearly interpolating the CMIP6 SSP (Shared Socioeconomic Pathway) 585 emission scenario between 2015 and 2020 (*29*). Emissions for 2016-2018 are derived by interpolating between 2015 and 2019, and those for 2020 are kept as given by SSP585 for the control simulation. Organic matter (OM) emissions are based solely on the CMIP6 historical and SSP585 inventories. Three perturbation simulations are created by reducing the anthropogenic SO_2, BC, and OM emissions over China for February, March and April 2020 by 20%, 40% or 60% to mimic the effects of COVID-19 lockdown. All other forcings (such as greenhouse gases, solar irradiance and stratospheric ozone) are based on the CMIP6 historical forcings (*14*) for 2000-2014 and the CMIP6 SSP585 forcings (*29*) for 2015-2020.

Supplementary Text

Analysis region

We more than double the original analysis region by expanding beyond EAMS further to the open ocean (the oceanic region in 117°–150°E and 26°–41°N). The results are qualitatively the same (Figs. S5 and S6). In fact, the model performs better in terms of the interannual variations of AOD and F_{clr}, reflecting the good agreement between the observed and simulated spatial structures (Figs. 1 and 3).

Long-term emission trends

As explained in the main text, the anthropogenic emissions over China have been varying non-monotonically in the last two decades, and despite our best effort, there are bound to be inherent uncertainties in the historical emission inventory used in the control simulation. To assess the implications, we re-run all the simulations with the emissions fixed at the 2000 levels. Doing so seriously degrades the model skills for AOD and F_{clr}, as the simulations clearly miss the observed long-term trends. These deficiencies tend to inflate the magnitudes of the forced signals for March 2020 (Figs. S7 and S8).

Locations of the emission reduction

The lockdown first started in Hubei Province before spreading to other parts of China. To study how the locations of the emission reduction affects the results, we divide the country roughly into northern China (NC, north of 35°N), central China (CC, 25°–35°N, where Hubei is located) and southern China (SC, south of 25°N), and reduce the emission by 60% for each region independently. AOD and F_{clr} are more sensitive to the reductions in NC and CC than in SC (Fig. S9). The same is true for F_{all} and cloud properties (Fig. S13). The spatial distributions are given in Figs. S10-12.

Speciation of the emission reduction

In the perturbation simulations, all three anthropogenic aerosol emissions, namely SO_2, BC. and OM, are reduced simultaneously. In a set of sensitivity experiments, we reduce one species by 60% at a time. SO_2 contributes the most to the reductions in AOD and F_{clr}. The effects of BC and OM on F_{clr} roughly cancel (Fig. S14). R_e increases most prominently in the SO_2 case (Fig. S15).

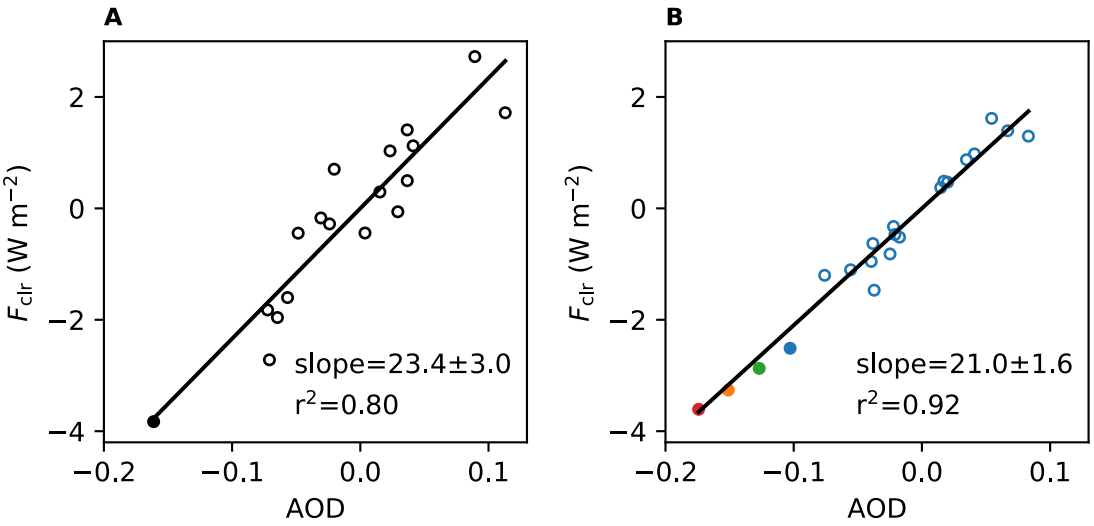

Fig. S1. Scatter plots of the anomalies in AOD and F_{clr} in March over EAMS. Open dots represent the climatological period (2003-2019) and solid dots represent the year 2020. (A) Observations from MODIS and CERES. (B) Blue dots are from the control model simulation. Orange, green, and red dots correspond to the 20%, 40% and 60% perturbation simulations, respectively. The regression line is calculated for the climatological period.

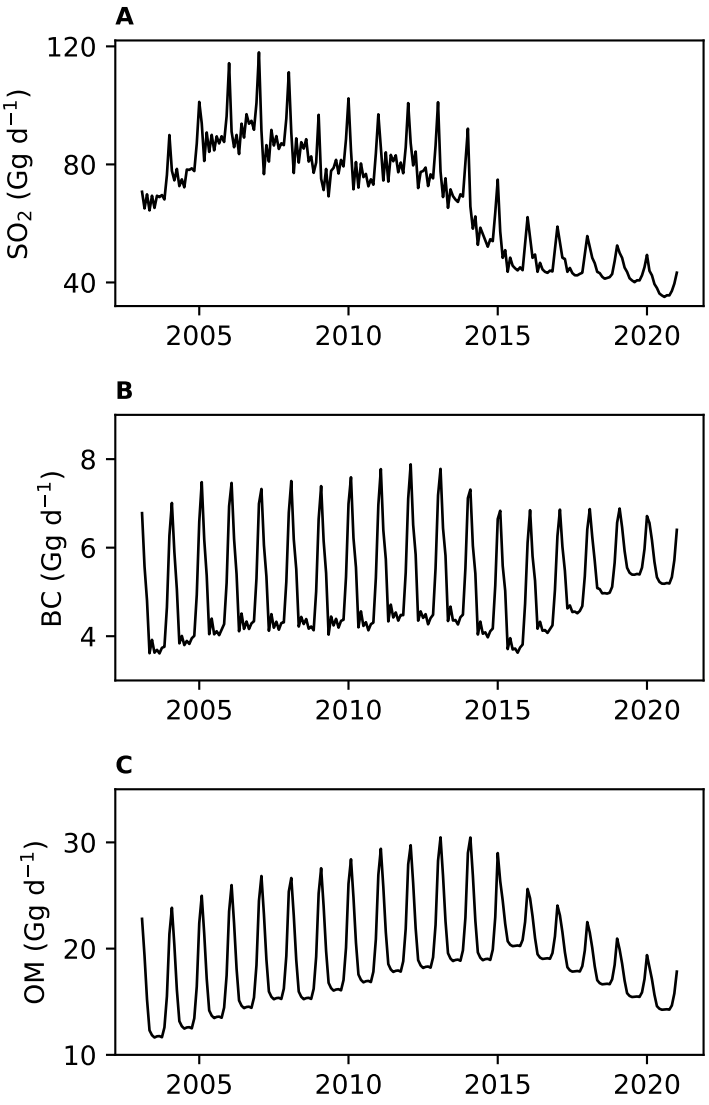

Fig. S2. Time series of monthly-mean anthropogenic emissions over China. (A) SO_2, (B) black carbon (BC), and (C) organic matter (OM).

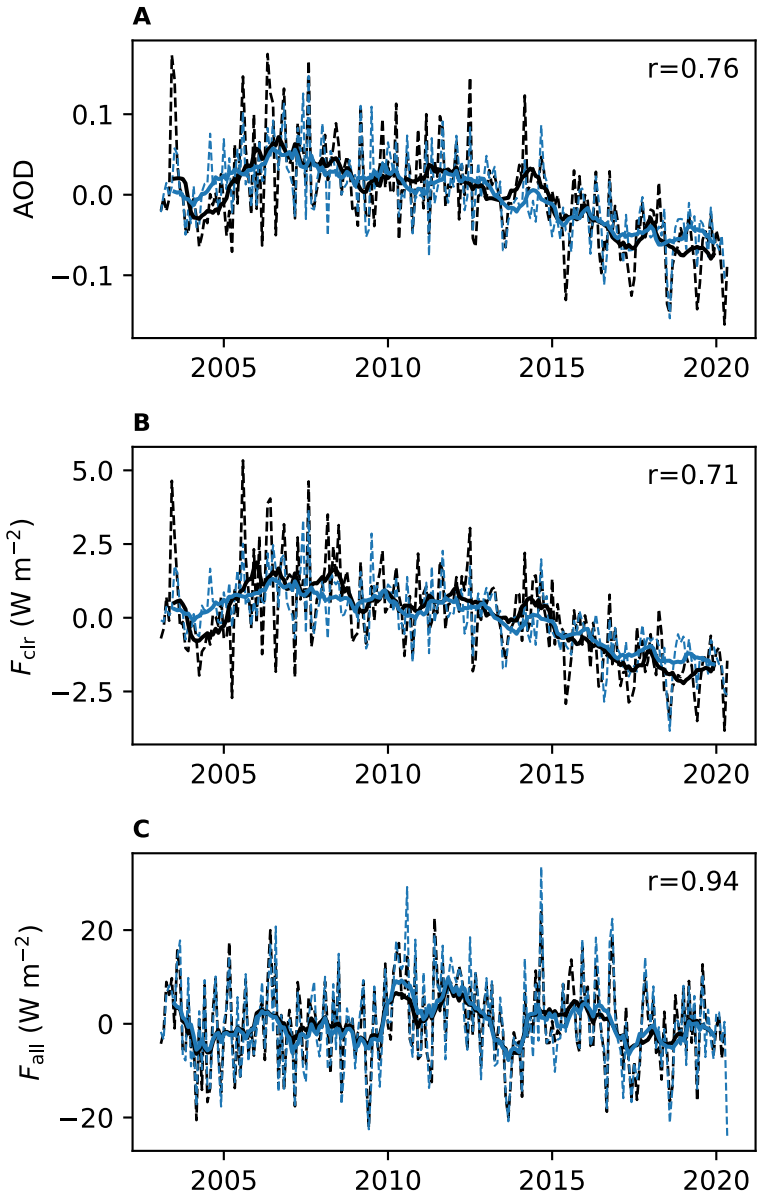

Fig. S3. Time series of monthly anomalies in (A) AOD, (B) F_{clr}, and (C) F_{all}. The black and blue lines represent the observations and the control simulation, respectively. The dotted and solid lines represent the monthly anomalies and 11-month running means, respectively. $\boldsymbol{r}$ is the correlation coefficient.

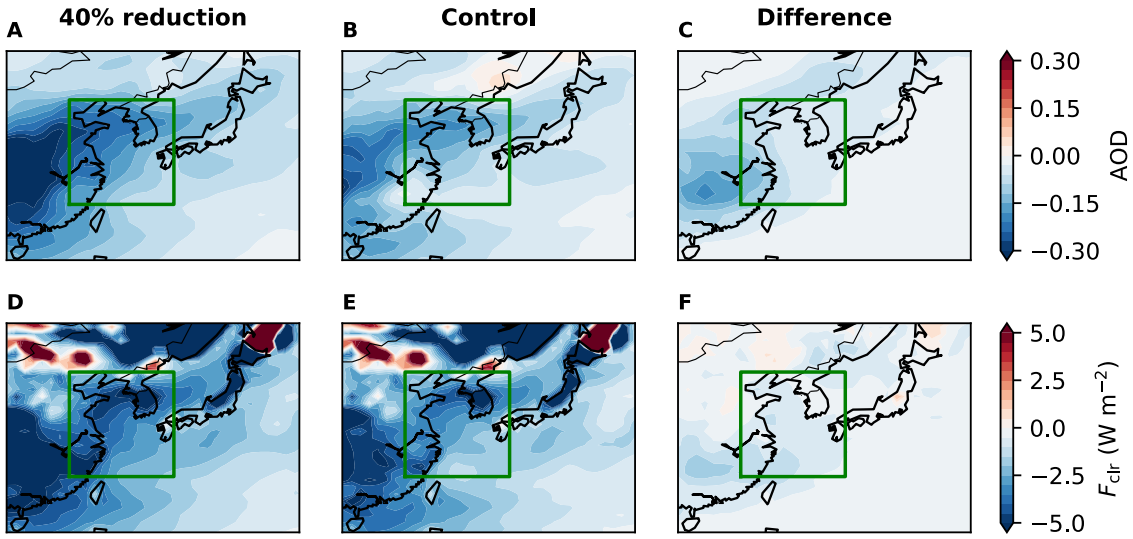

Fig S4. Same as Fig. 3, but for the 40% perturbation simulation.

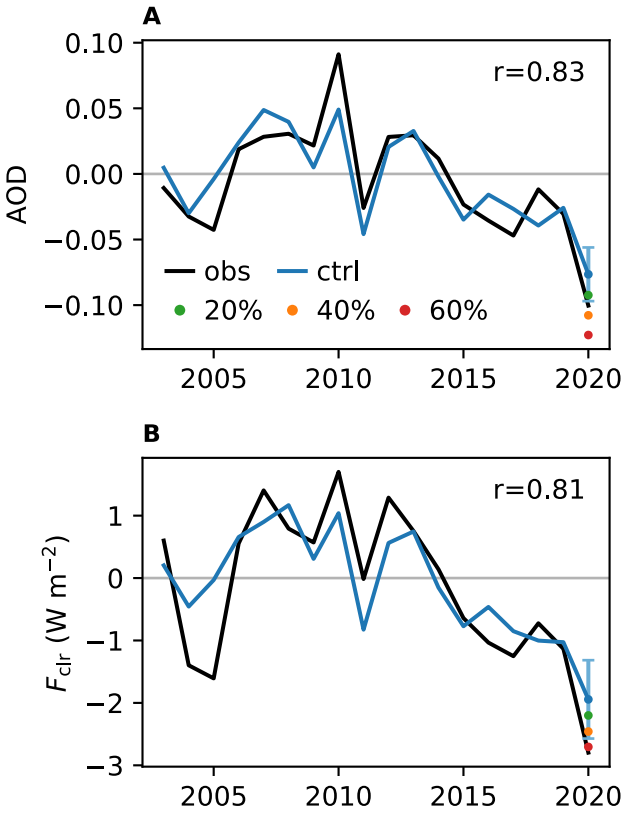

Fig S5. Same as Fig. 2, but for the expanded oceanic region from 117°–150°E and 26°–41°N.

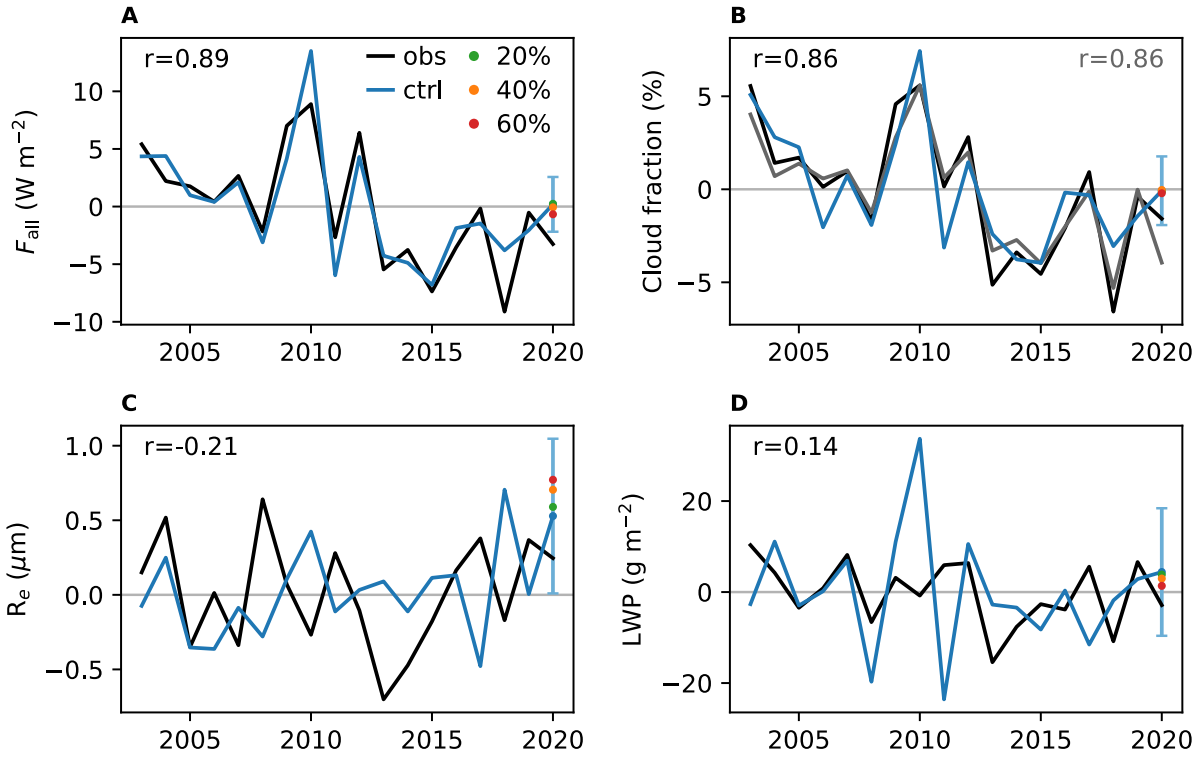

Fig S6. Same as Fig. 4, but for the expanded oceanic region from 117°–150°E and 26°–41°N.

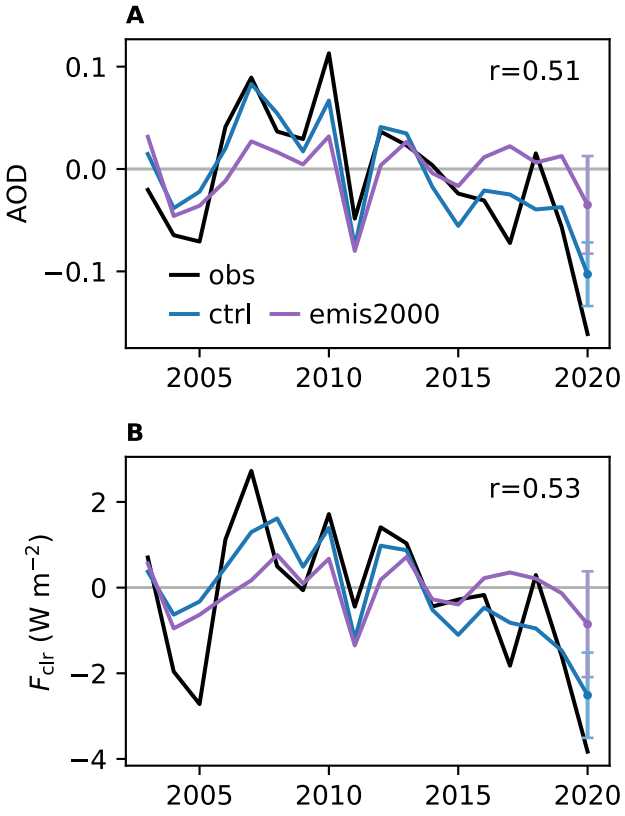

Fig S7. Same as Fig. 2, but for the constant emission simulation (the purple line). The blue line is from the control simulation. r is the correlation coefficient for the constant emission simulation.

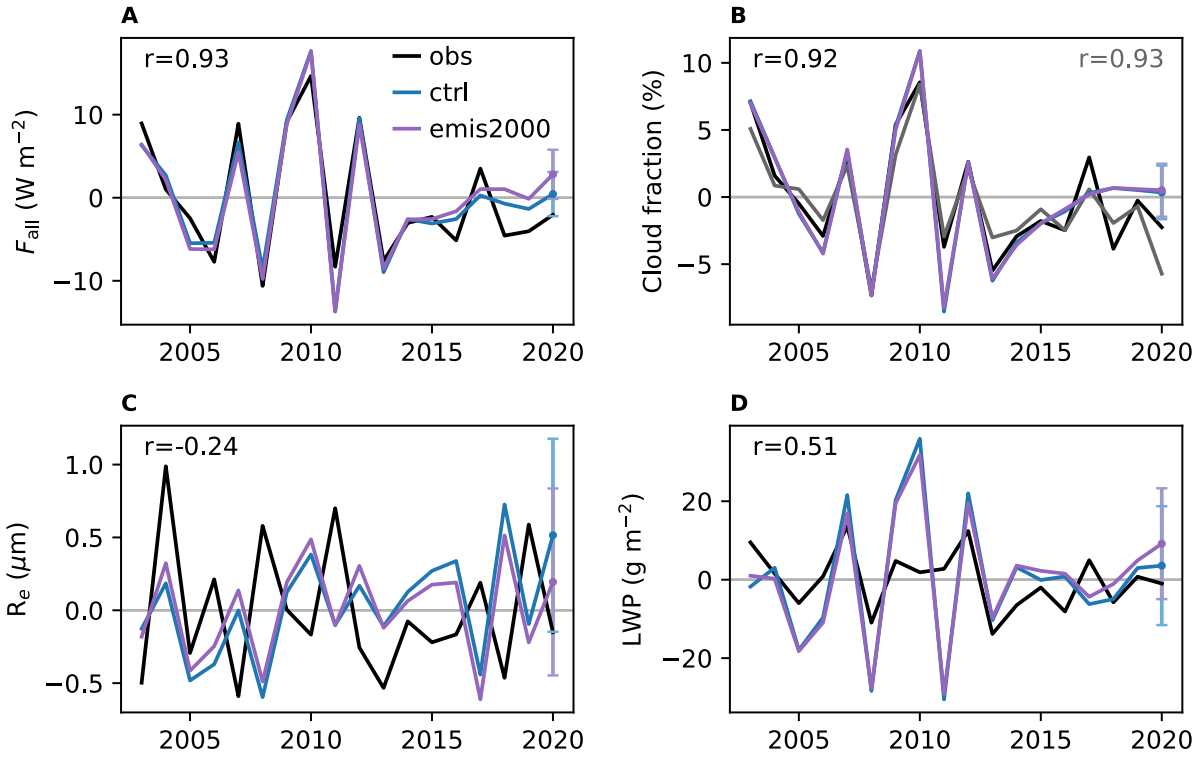

Fig S8. Same as Fig. 4, but for the constant emission simulation (the purple line). The blue line is from the control simulation. r is the correlation coefficient for the constant emission simulation.

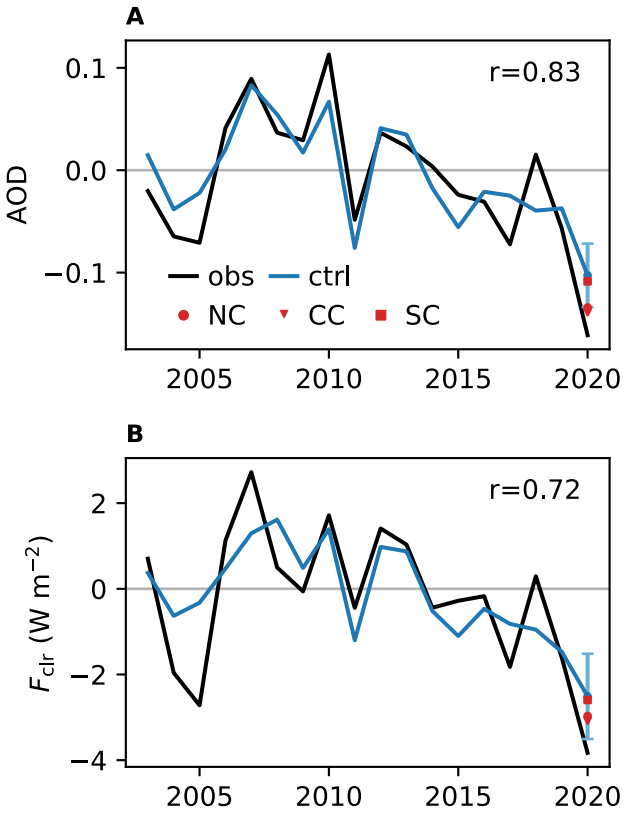

Fig S9. Same as Fig. 2, but for the emission location simulations. NC, CC, and SC represent northern China (north of 35°N), central China (25°–35°N) and southern China (south of 25°N), respectively. The regional emissions reduction is 60%.

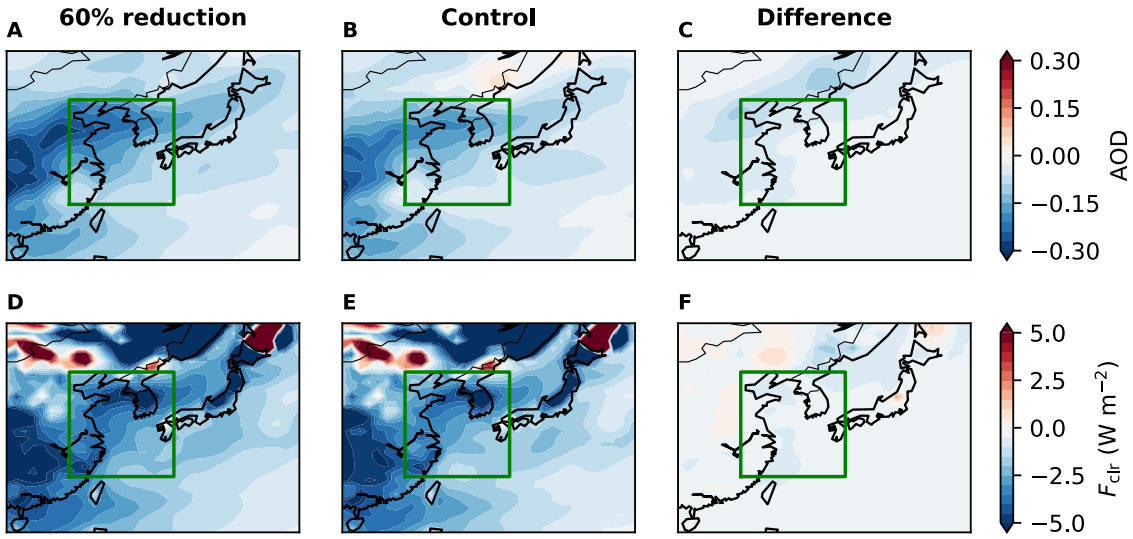

Fig S10. Same as Fig. 3, but for the northern China (NC) emission location simulation. The regional emissions reduction is 60%.

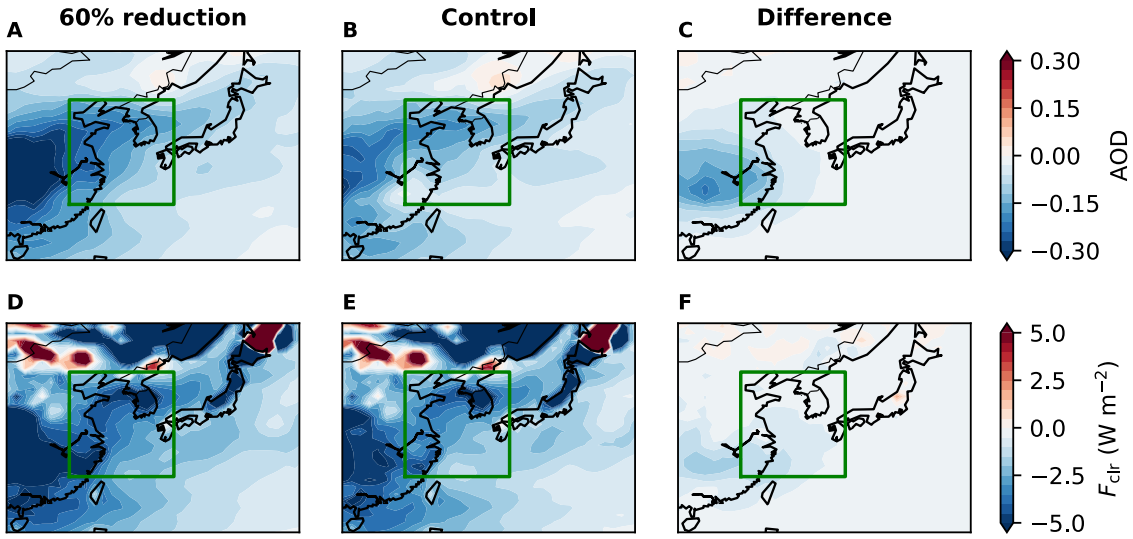

Fig S11. Same as Fig. 3, but for the central China (CC) emission location simulation. The regional emissions reduction is 60%.

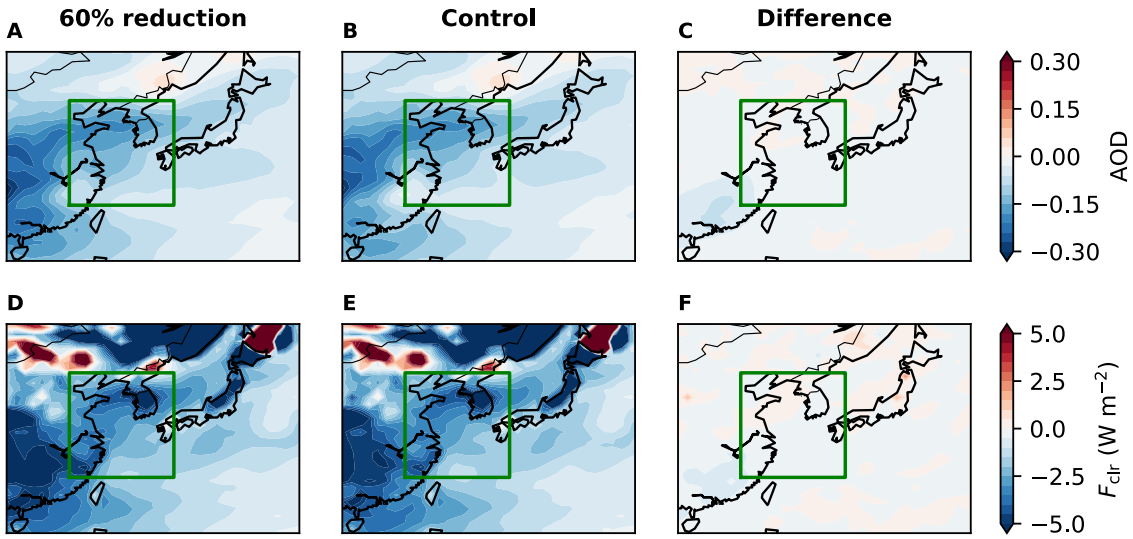

Fig S12. Same as Fig. 3, but for the southern China (SC) emission location simulation. The regional emissions reduction is 60%.

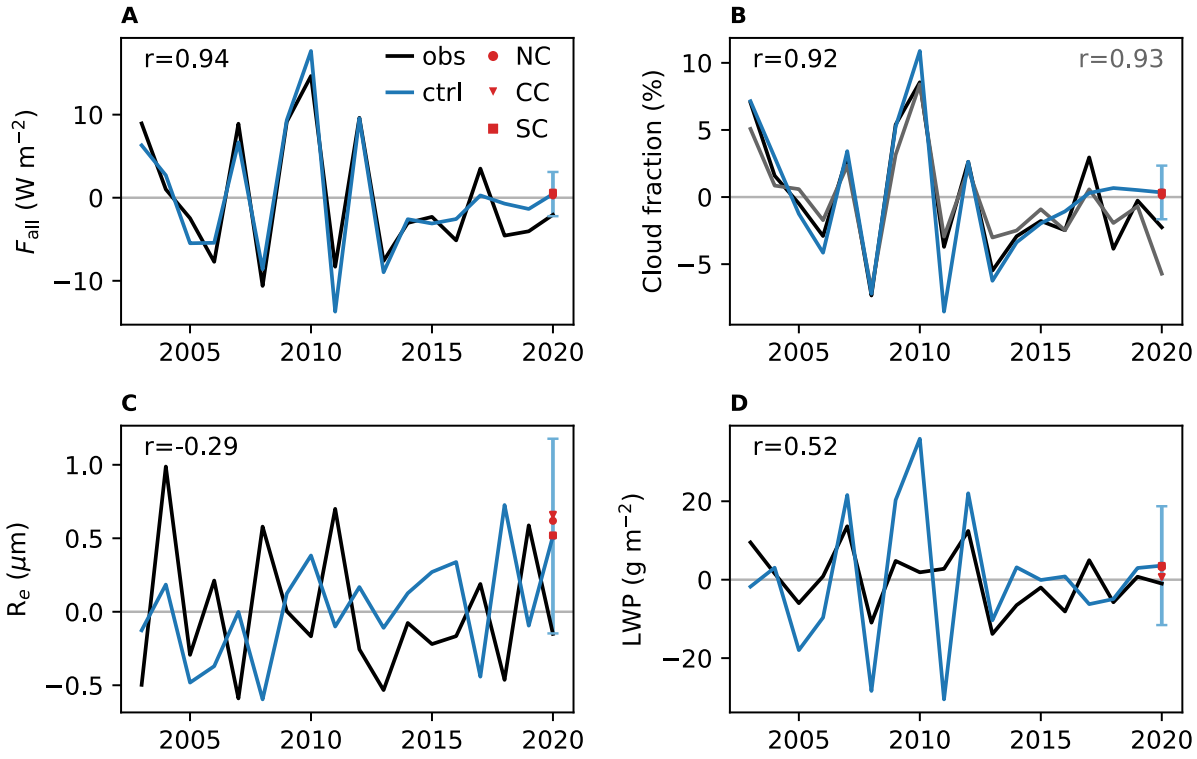

Fig S13. Same as Fig. 4, but for the emission location simulations. NC, CC, and SC represent the northern China (north of 35°N), central China (25°–35°N) and southern China (south of 25°N), respectively. The regional emissions reduction is 60%.

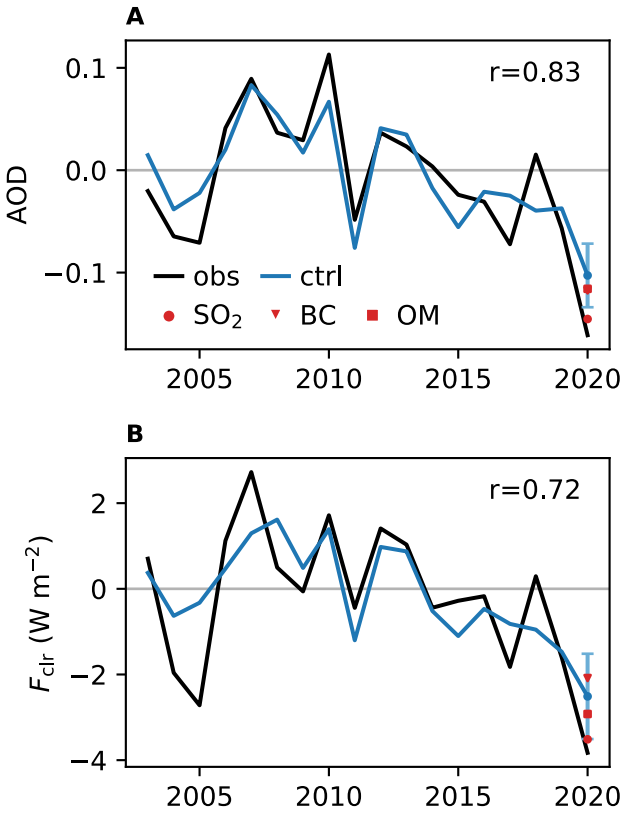

Fig S14. Same as Fig. 2, but for the emission speciation simulations. The emission reduction is 60%.

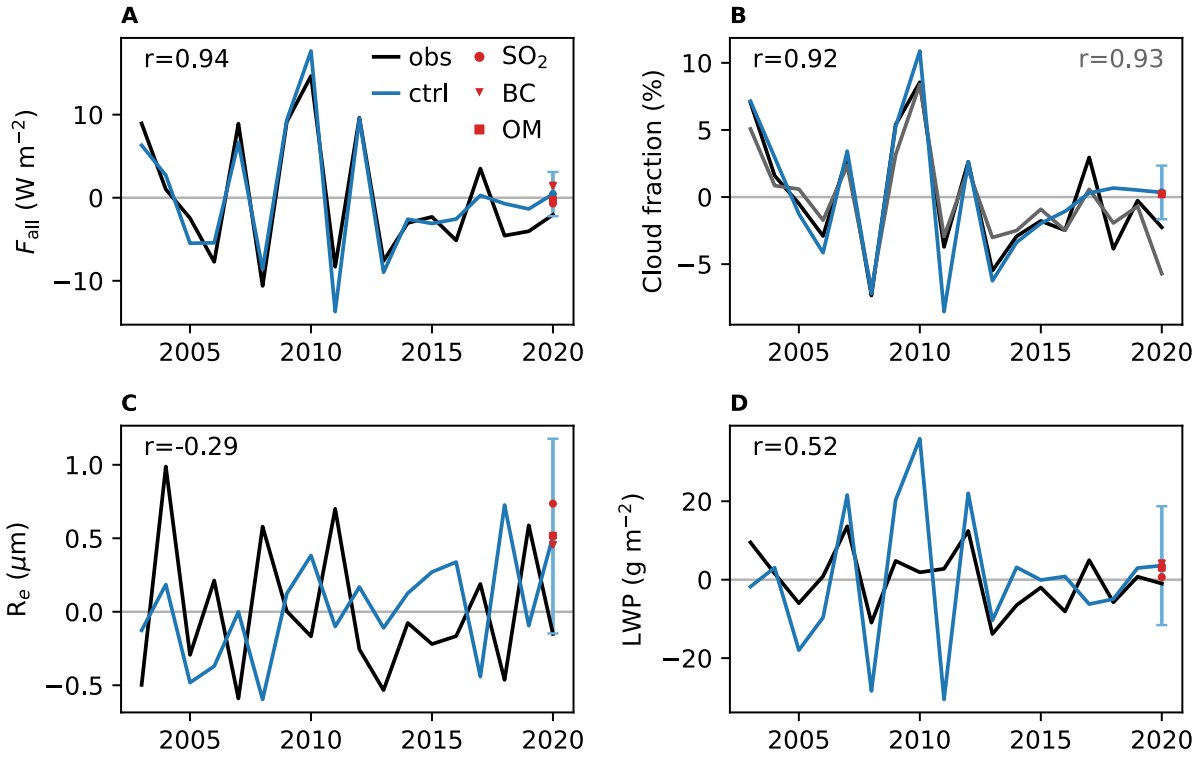

Fig S15. Same as Fig. 4, but for the emission speciation simulations. The emission reduction is 60%.

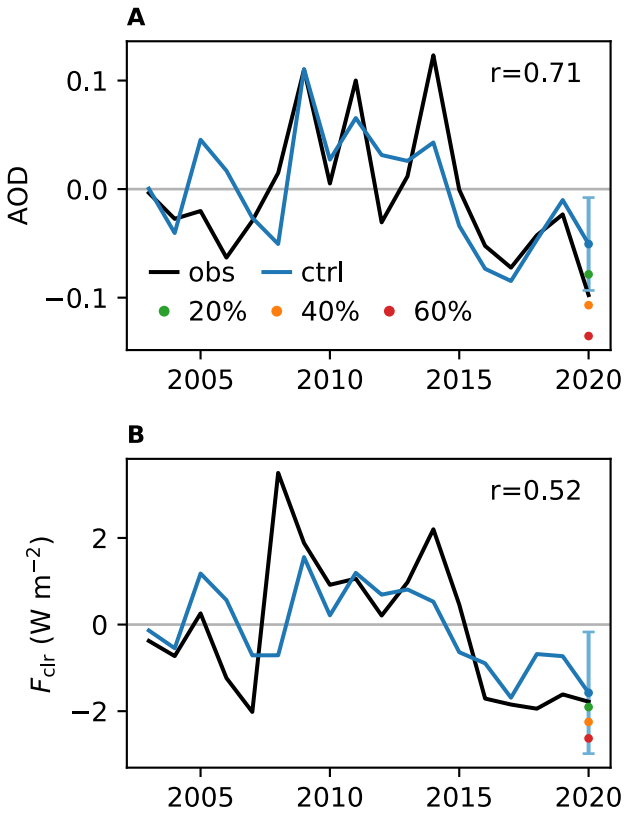

Fig. S16. Same as Fig. 2, but for February.

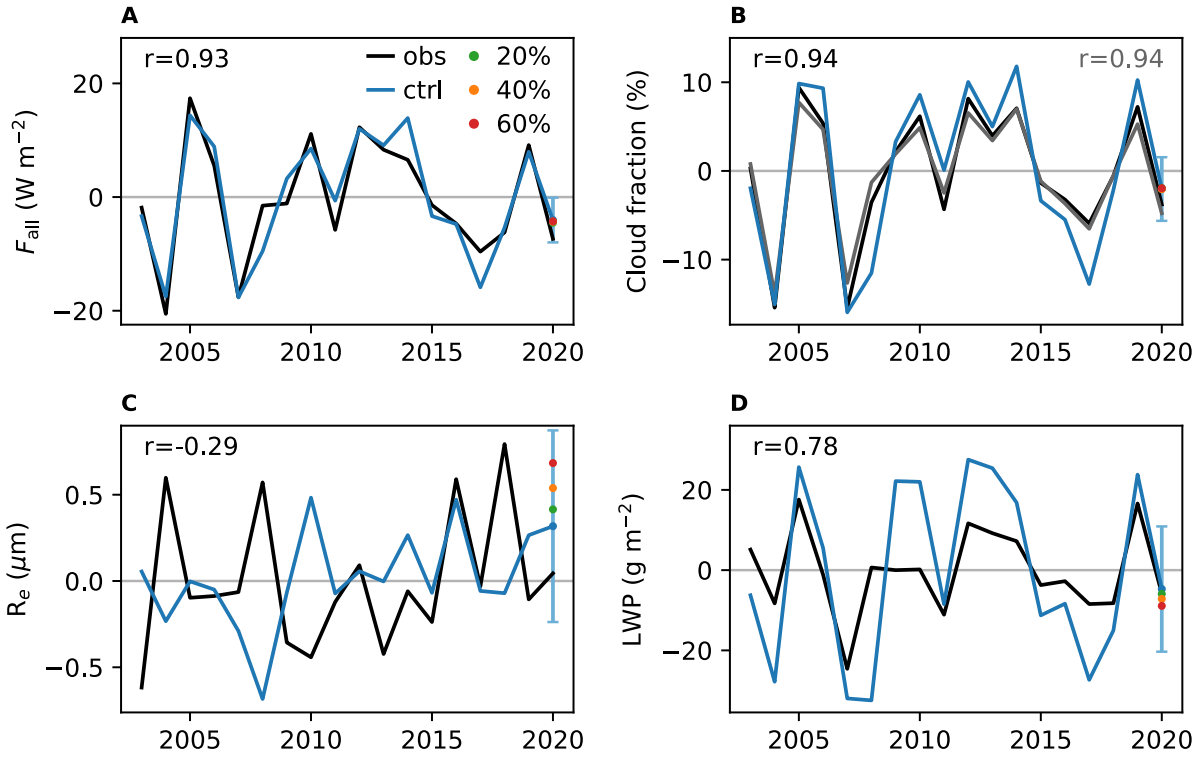

Fig. S17. Same as Fig. 4, but for February.

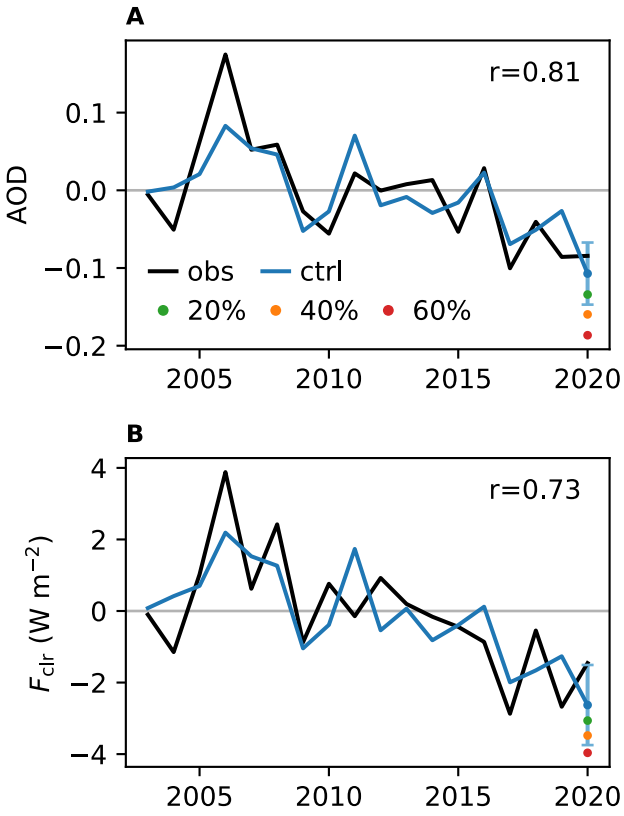

Fig. S18. Same as Fig. 2, but for April.

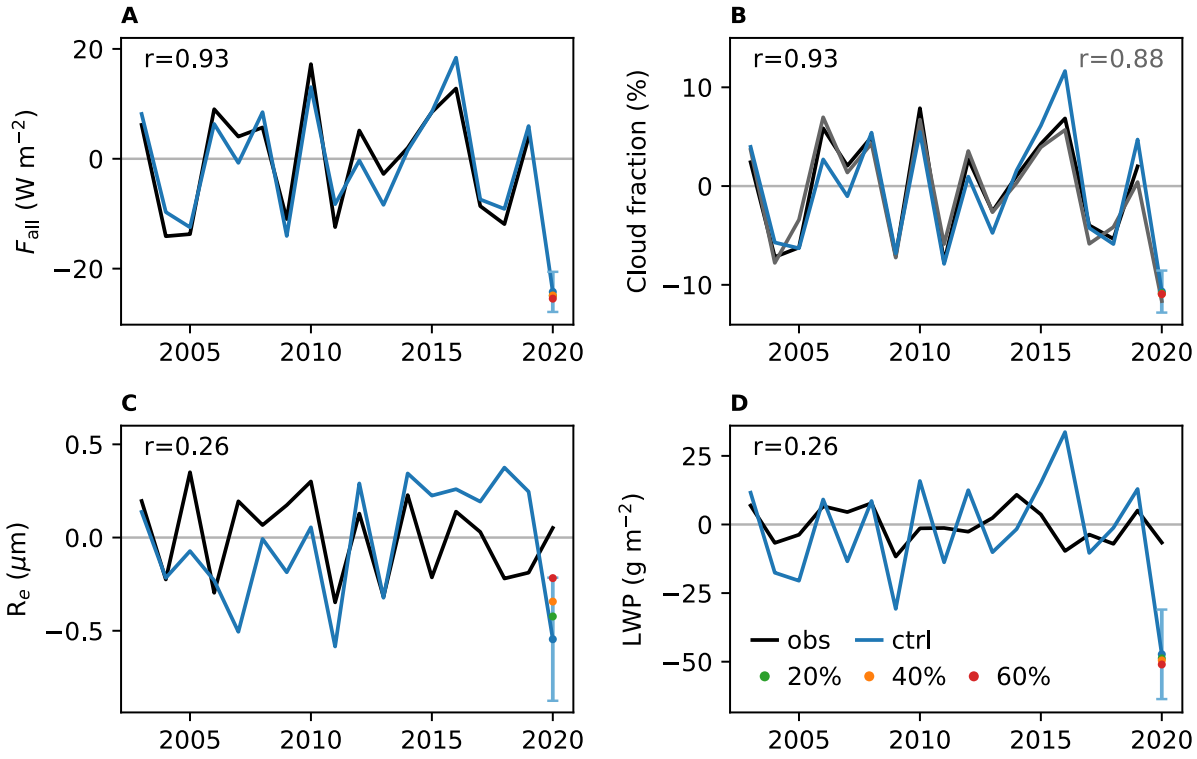

Fig. S19. Same as Fig. 4, but for April.